AD-A181 204 ACTA AERONAUTICA ET ASTRONAUTICA SINICA (SELECTED ARTICLES)(U) FOREIGN TECHNOLOGY DIV WRIGHT-PATTERSON AFB OH 18 MAY 87 FTD-ID(RS)T-0117-86 1/1

UNCLASSIFIED F/G 20/4 NL

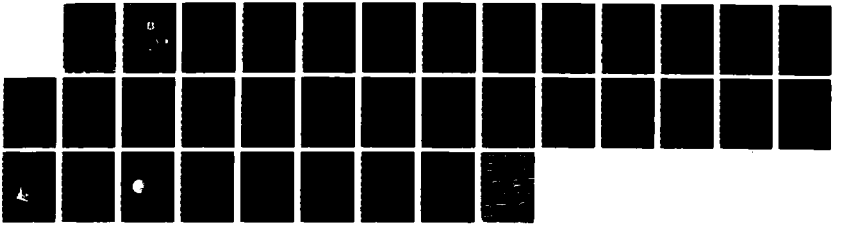

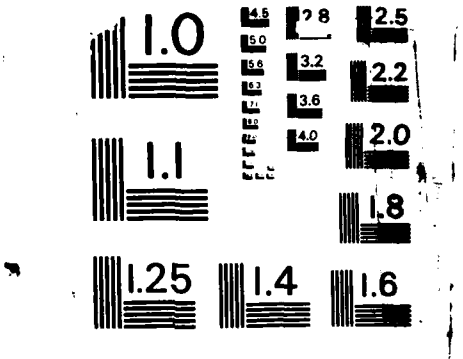

MICROCOPY RESOLUTION TEST CHART
NATIONAL BUREAU OF STANDARDS-1963-A

(2)

FTD-ID(RS)T-0117-87

FOREIGN TECHNOLOGY DIVISION

ACTA AERONAUTICA ET ASTRONAUTICA SINICA

(Selected Articles)

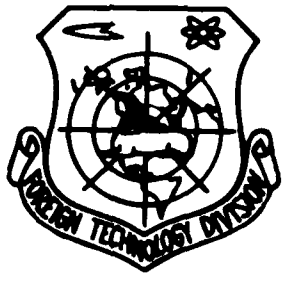

Approved for public release;
Distribution unlimited.

HUMAN TRANSLATION

FTD-ID(RS)T-0117-87 18 May 1987

MICROFICHE NR: FTD-87-C-000356

ACTA AERONAUTICA ET ASTRONAUTICA SINICA (Selected Articles)

English pages: 29

Source: Hangkong Xuebao, Vol. 7, Nr. 2, April 1986, pp. 205-216

Country of origin: China
Translated by: SCITRAN
F33657-84-D-0165
Requester: FTD/TQTA

PREPARED BY

TRANSLATION DIVISION
FOREIGN TECHNOLOGY DIVISION
WPAFB OHIO

TABLE OF CONTENTS

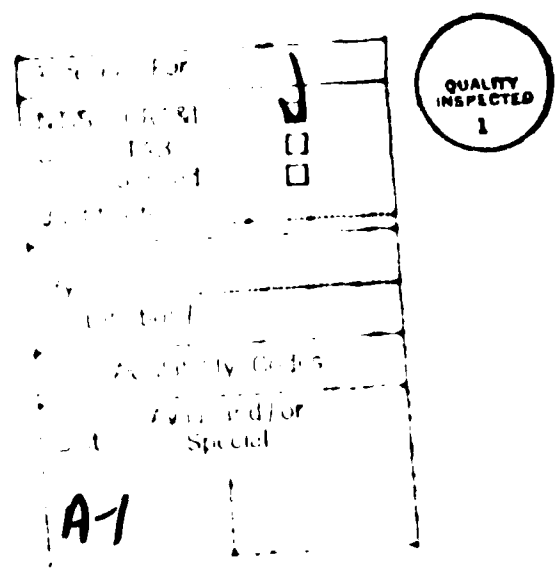

GRAPHICS DISCLAIMER

All figures, graphics, tables, equations, etc. merged into this translation were extracted from the best quality copy available.

CALCULATIONS OF STEADY AND UNSTEADY TRANSONIC FLOWS OVER AIRFOILS BY MONOTONE SWITCH

Ang Haisong and Cheng Zhonglu
Shengyang Research Institute of Aerodynamics

1. INTRODUCTION

When calculating transonic unsteady potential flows, scientists are continuously seeking improved methods for solving non-linear problems which include shock-wave movement, and for increasing the efficiency of calculation. In 1977, Ballhaus and Goorjian [1] succeeded in solving the time-field unsteady transonic small-disturbance equations by using alternative-direction implicit-difference method (ADI), and this method was called LTRAN2. Reference [5] also carried out a study, which is similar to LTRAN2, by introducing a coordinate transformation. Since then, several authors [2] have confirmed through numerical experiments that the suitable frequency range of the LTRAN2 method can be expanded by using a time-correlation term to improve the original quasi-steady boundary conditions. In

---

Received October 4, 1984.

1981, Goorjian and Buskirk [3] improved the Murman-Cole-type switch by using the Engquist-Osher-type monotone switch, and proved that its efficiency is higher and the stability is better. They eliminated the possibility of existing expansive shock-wave non-isentropic solutions which were permitted by the original switch.

In order to increase the efficiency of calculation and expand the applicable range, we have introduced an E-O-type ADI-difference switch, the body-surface and tail-vortex-surface boundary conditions with an additional time-derivative term, and a pressure-coefficient formula. In order to reduce the region of calculation and avoid the inconvenience of coordinate transformation, the unsteady non-reflective boundary conditions [4] and steady asymptotic solution were used. A set of programs for calculating steady and unsteady flows using main equations having the same forms were established. The numerical experiments have shown that this is a cost-effective method for calculating two-dimensional transonic unsteady flows with certain precision and applicable scope.

2. BASIC EQUATION AND BOUNDARY CONDITIONS

The main equation.

The equation of two-dimensional unsteady transonic small-disturbance flows (under the assumption of low frequency) can be written in the following form:

$$(-2ikMa_\infty\varphi_x)_x+\left[(1-Ma_\infty^2)\varphi_x-\frac{1}{2}(\gamma+1)Ma_\infty^m\varphi_x^2\right]_x+(\varphi_y)_y=0 \qquad (1)$$

Here the coordinates x, y, time t, and the disturbance speed-potential φ are already non-dimensionalized by c, ω^{-1} and cU_∞ (c is the chord length, ω is the frequency), and the simplified frequency $k=\omega c/U_\infty$. Exponent m is taken according to the series expansion analysis of the precise formula of critical pressure coefficient of isentropic flows, that is: the corrected value which satisfies: $2>m>\frac{2\gamma+1}{\gamma+1}$

The boundary conditions on the body surface. ($y=f(x,t)$)

The condition stating that the relative velocity of air flow is tangent to the instantaneous body surface is:

$$\varphi_y=f_x+kf_t \qquad (2)$$

For the resonant situation, the boundary condition at the wing surface can be written as:

$$\varphi_y=h_x-\alpha_0+\alpha_1\sin(\omega t)+\alpha_1 k(x-x_0)\cos(\omega t) \qquad (3)$$

where h=h(x) is the geometric shape of body surface, α_0 is the attack angle at the average position, α_1 is the amplitude of unsteady movement.

The pressure coefficient of unsteady flows is:

$$C_p = -2(\varphi_x + k\varphi_t) \tag{4}$$

The boundary conditions on the surface of the tail-vortex:

According to the Kutta condition, on the surface of tail vortex, we have:

$$\Delta\varphi_t = (\varphi_t)_+ - (\varphi)_T = 0 \tag{5}$$

$$\Delta C_p = \Gamma_x + k\Gamma_t = 0 \tag{6}$$

where the circulation of the tail vortex $\Gamma(x,t)=\Delta\varphi(x,t)_{tail}$. Formula (6) reflects the characteristic of the downward propagation of the tail vortex.

The far-field condition of unsteady flows:

At the far-upstream and far-downstream positions, we use the Engquist-Majda non-reflective far-field boundary condition

$$\varphi_t \pm \sqrt{|1 - Ma_\infty^2 - (\gamma+1)Ma_\infty^2\varphi_x|}\,\varphi_x = 0 \tag{7}$$

At the upstream-front, we take $\varphi=0$ at the positions which are far enough and go to the boundary of the upstream-front by interpolating. Downstream , under the assumption that the disturbance pressure is zero, we have:

$$\varphi_x+k\varphi_t=0 \tag{8}$$

The equation and conditions for steady flows:

The main equation is the same as equation (1). Only the first term coefficient of the iterated parameter is changed. The boundary conditions at the body surface and the tail vortex surface are those given above by eliminating the derivative term of t. The far-field condition is an asymptotic solution of the velocity potential of the disturbance.

$$\varphi=\frac{\Gamma}{2\pi}\left[\frac{\pi}{2}sgn(y)+\tan^{-1}\left(\frac{x}{\beta y}\right)\right]+\frac{1}{\pi\beta}\frac{x}{x^2+\beta^2y^2}\int_c F(\xi)d\xi+\varphi_{base} \tag{9}$$

where $\beta=\sqrt{1-Ma_\infty^2}$, and F(ξ) is the thickness function of the body surface.

The initial condition:

For the initial condition of unsteady flows we take the result of steady flow calculation:

$$\varphi(x,y,0)=\varphi_{ss}(x,y) \tag{10}$$

3. DIFFERENCE SWITCH

After the differencing of equation (1), the equation can be rewritten as an alternate implicit form which uses double-step calculation for each time step:

In x direction:

$$2kM a_\infty^2 (\Delta t)^{-1} \delta_x (\tilde{\varphi}_{i,j} - \varphi^n_{i,j}) = D_x f + \delta_{yy} \varphi^n_{i,j} \tag{11a}$$

In y direction:

$$2kM a_\infty^2 (\Delta t)^{-1} \delta_x (\varphi^{n+1}_{i,j} - \tilde{\varphi}_{i,j}) = -\frac{1}{2} \delta_{yy} (\varphi^{n+1}_{i,j} - \varphi^n_{i,j}) \tag{11b}$$

Here:

$$D_x f = \vec{\Delta}_x f + \overleftarrow{\Delta}_x f \tag{12a}$$

$$\vec{\Delta}_x f = (f_{i+\frac{1}{2},\, j} - f_{i-\frac{1}{2},\, j}) [1/2 (x_{i+1} - x_{i-1})]^{-1} \tag{12b}$$

$$\overleftarrow{\Delta}_x f = (f_{i-\frac{1}{2},\, j} - f_{i-\frac{3}{2},\, j}) [1/2 (x_{i+1} - x_{i-1})]^{-1} \tag{12c}$$

$$f_{i-\frac{1}{2},\, j} = 1/2 [c_1 \hat{u}_{i-\frac{1}{2},\, j} + (c_1 + c_2 \hat{u}_{i-\frac{1}{2},\, j}) (\tilde{\varphi}_{i,j} - \tilde{\varphi}_{i-1,j}) (x_i - x_{i-1})^{-1}] \tag{12d}$$

$$c_1 = 1 - M a_\infty^2, \quad c_2 = -(\gamma + 1) M a_\infty^2, \quad \hat{u} = -c_1/c_2 \text{ (Sound Speed of disturbance)} \tag{12e}$$

$$\hat{u}_{i-\frac{1}{2},\,j}\begin{cases}=\max(u_{i-\frac{1}{2},\,j},\ \bar{u}) & (\text{in } \overleftarrow{\Delta}_x f)\\ =\min(u_{i-\frac{1}{2},\,j},\ \bar{u}) & (\text{in } \overleftarrow{\Delta}_x f)\end{cases} \tag{12f}$$

$$\delta_x\varphi^n_{i,j}=(\varphi^n_{i,j}-\varphi^n_{i-1,j})\left[1/2\,(x_{i+1}-x_{i-1})\right]^{-1} \tag{12g}$$

$$\delta_{yy}\varphi_{i,j}=(\overleftarrow{\delta}_y\varphi_{i,j+1}-\overleftarrow{\delta}_y\varphi_{i,j})\left[1/2\,(y_{j+1}-y_{j-1})\right]^{-1} \tag{12h}$$

$$u_{i-\frac{1}{2},\,j}=\overleftarrow{\delta}_x\varphi^n_{i,j} \tag{12i}$$

Here, $\overleftarrow{\delta}_x$ and $\overleftarrow{\delta}_y$ are first order backward difference operators. The above E-O-type correlation switch has the following monotonic character:

$$(\partial u^{n+1}_i/\partial u_{i\pm1}^{n+\theta})>0 \tag{13}$$

therefore it has better stability and convergence.

The switch difference of the non-reflective far-field boundary is:

$$\overleftarrow{\delta}_y\varphi^{n+\frac{1}{2}}_{i-\frac{1}{2},\,j+\theta+1}\pm|c_1+c_2\overleftarrow{\delta}_x\varphi^n_{i,\,j\mp\frac{1}{2}}|^{\frac{1}{2}}\overleftarrow{\delta}_x\varphi^{n+\frac{1}{2}}_{i,\,j\mp\frac{1}{2}}=0 \tag{14}$$

By using different "following methods" to obtain the solutions, the four- and three-diagonal algebra equation groups can be obtained.

4. EXAMPLES AND ANALYSIS

Steady-flow calculation:

We have calculated the steady flows for several wing types and several Ma_∞. Fig. 1 shows the calculated results and a comparison for one of the calculations. It can be seen that the results of this method is closer to the experimental data. The standard for convergence is: the maximum difference of velocity potential $|\varphi^{n+1}_{i,j} - \varphi^{n}_{i,j}|_{max} < 10^{-4}$; the iteration takes 300 ~ 520 steps. The non-uniform network of the calculated space is (44X35) and (50X35) in a physically rectangular coordinate system, $|y|_{max} \leqslant 6c$, $|x|_{max} \leqslant 5c$.

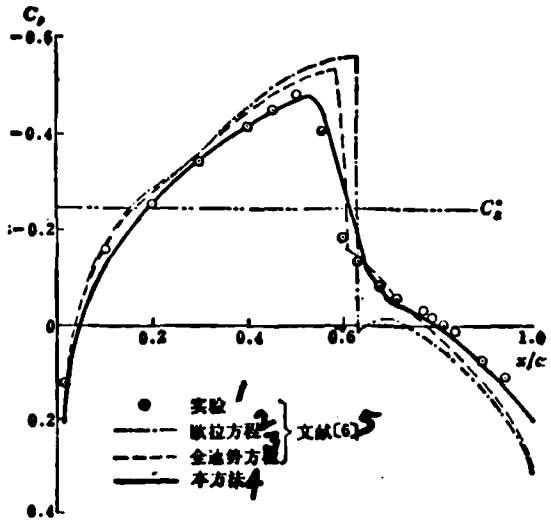

Fig. 1. The steady pressure coefficient of NACA64A006-type wings, $Ma_\infty=0.785$, $\alpha_0=0°$.

1 - experiment; 2 - the Euler equation; 3 - full-potential-velocity equation; 4 - this method; 5 - reference (6).

Side-wing vibration.

We have carried out a numerical computation test with and without the unsteady term in the boundary conditions and have found that: when the term of the derivative of t is included, the calculated results were not influenced even when the time steps were enlarged; whereas when the derivative term of t was not included, under the condition of the same time step, the calculated results of convergence will be faulty solutions which vibrate near the shock waves.

(Fig. 2 shows the situation at a certain moment, and it is similar for other moments.) Therefore we have found that with or without the term of the derivative of t, not only is the range of frequency correlated, but also the correctness of the calculation will be influenced.

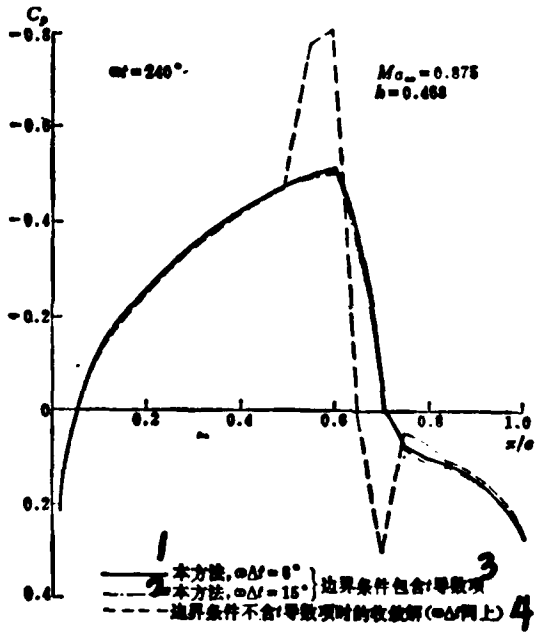

Fig. 2. The pressure coefficient of $a_{\wedge}^{(1°\sin \omega t)}$NACA64A006-type wing with 1/4 vibrating side wings.

1 - this method; 2 - this method; 3 - boundary conditions contain the term of the derivative of t; 4 - convergence solution when the boundary condition does not include the term of the derivative of t.

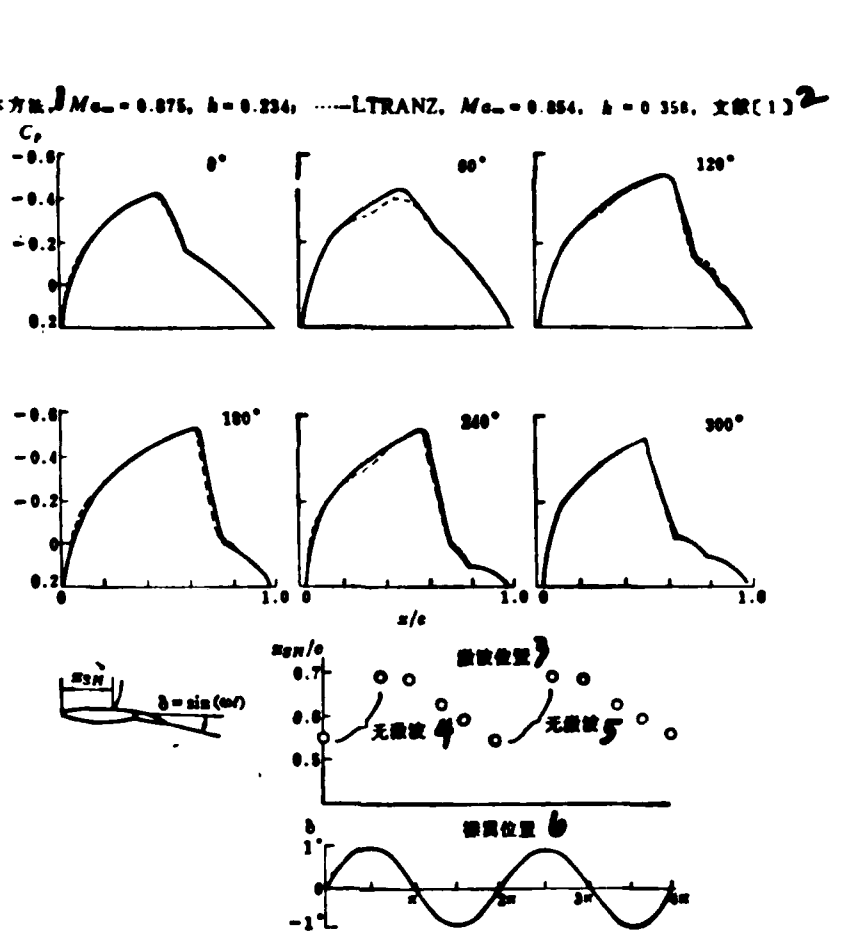

Fig. 3. The unsteady pressure coefficient of a NACA64A006-type wing with vibrating side wings (the shock-wave movement is B-type).

1 - this method; 2 - reference [1]; 3 - shock-wave position; 4 - no shock wave; 5 - no shock wave; 6 - side-wing position.

LTRAN2 has simulated three types of the periodic movement shock waves found by the experiment of Tijdeman [6]. But this is only a qualitative simulation (see Table 1).

Table 1. Experimental and calculated conditions of oscillation of wing flap with NACA64A006 airfoil.

[illegible] 1	A 4		B 5		C 6	
	Ma_∞	k	Ma_∞	k	Ma_∞	k
Tijdeman [illegible] 2	0.8	0.228	0.875	0.284	0.85	0.240
LTRAN2 [illegible] 3	0.875	0.468	0.854	0.368	0.822	0.496

1 - type of shock wave movement; 2 - the Tijdeman experiment; 3 - LTRAN2 calculation; 4 - A-type; 5 - B-type; 6 - C-type.

In the simulation of the three shock-wave movement with this method, we have found that when the Ma_∞ and k conditions are directly taken from the Tijdeman experiment, The same curve pattern of shock-wave movement resulted (Fig. 3 gives the results for B-type), and the results are compared with the experimental results (Fig. 4). Therefore, the simulation of this method is consistent quantitatively with the experimental results.

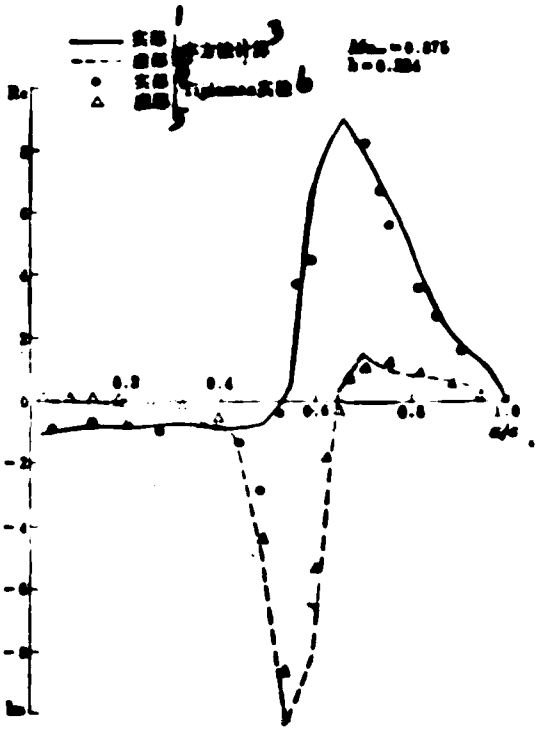

Fig. 4. A comparison of the calculated results and the experimental results of the unsteady pressure coefficients in the vibration of side wings (NACA64A006).
1 - real part; 2 - imaginary part; 3 - calculated by using this method; 4 - real part; 5 - imaginary part; 6 - the Tijdeman experiment.

Pitching vibration.

We mainly investigated the vibration situation of the all-wing type for higher simplified frequencies. The results of the real parts (given in Fig. 5(a)) agree well. From the results of the

imaginary parts in Fig. 5(b), it can be seen that the relative errors of the results in this method compared to the experimental results are less than in the LTRAN2 method. This shows that when the frequency increases, the improvement of the unsteady term is mainly reflected in the imaginary parts which indicate the changes of phase lag of unsteady pressure, and this will influence the magnitude of the torque. The relation between the time-field pressure coefficient and the real and imaginary parts of the frequency-field is:

$$\Delta C_p = a_1[Re\sin(\omega t) + Im\cos(\omega t)] \tag{15}$$

where Re is the real part and Im is the imaginary part.

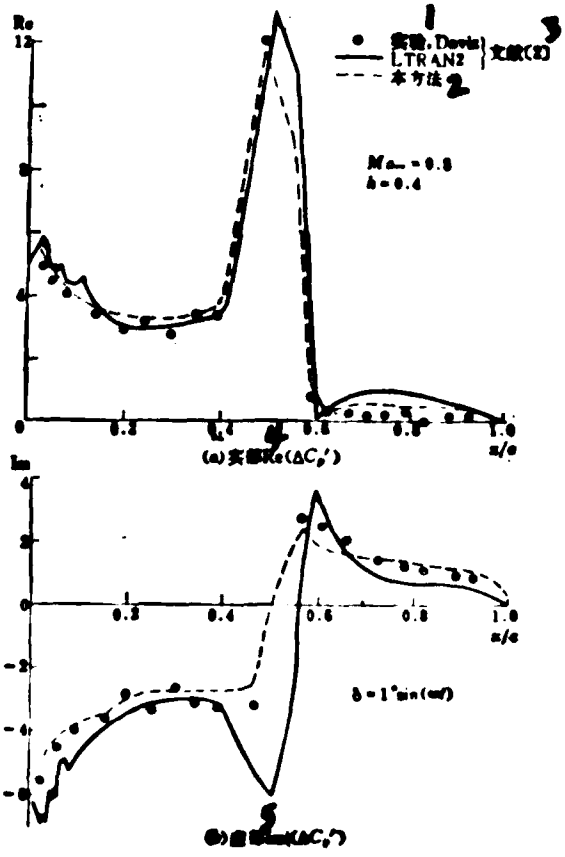

Fig. 5. The unsteady pressure coefficient of the NACA64A010-type wing in pitching vibration (x/c=0.25). 1 - experiment; 2 - this method; 3 - reference [2]; 4 - real part; 5 - imaginary part.

In this method, the time step used in the unsteady-flow calculation is usually 2 ~ 5 times larger than in L TRAN2 method ($\omega\Delta t$=6° ~15°). The calculation is stable and the region of calculation is smaller (same as the above network used in steady flows). Therefore the computer time can obviously be reduced. The convergence standard of the

unsteady calculation was taken $[\Delta v]_{max} < 10^{-3}$. Usually 3 ~ 6 circulations are required to reach the standard.

Our work has obtained the sincere help of Professor Lu Shijun and Comrade Li Jungfu. The authors would like to thank them.

REFERENCES

[1] Ballhaus, W. F. and Goorjian, P. M., Implicit Finite Difference Computations of Unsteady Transonic Flows about Airfoils Including the Treatment of Irregular Shock Wave Motions, AIAA J., vol. 15, No. 12, (1977), pp. 1728-1735.

[2] Hessenius, K. A. and Goorjian, P. M., A Validation of LTRAN2 with High Frequency Extensions by Comparisons with Experimental Measurements of Unsteady Transonic Flows, NASA TM-81307, (1981).

[3] Goorjian P. M. and Buskirk R. V., Implicit Calculations of Transonic Flows Using Monotone Methods, AIAA 81-331, (1981).

[4] Kwak, D., Nonreflecting Far-Field Boundary Conditions for Unsteady Transonic Flow Computation, AIAA J., vol.

19, No. 11, (1981), pp. 1401-1407.

[5] Lu Huiming and Chang Jianbai, The calculations of Transonic Unsteady Flows of Two-dimensional Wings, Chinese J. Aerodynamics, No. 3, (1983), pp. 95-99.

[6] Tijdeman, H., Investigations of the Transonic Flow around Oscillating Airfoils, NLR TR 77090U.

Abstract

A numerical method for calculation of two-dimensional, inviscid, steady and unsteady, small-disturbance transonic flows is presented. A monotone switch ADI algorithm is used to solve the governing equation. The appropriate unsteady terms are added to the boundary conditions on body surface and wake. An analytical, asymptotic solution and the nonreflecting far-field boundary conditions are chosen for steady and unsteady case, respectively. A nonumiform mesh spacing and relatively large time-step are allowable. The developed computer program can be applied for solving both the steady and unsteady flows. Hence, it can be more efficient to use.

The computational results obtained from the present method for some examples have provided a closer agreement with experimental results compared to other methods.

APPLICATION OF DUAL HOLOGRAM INTERFEROMETRY TO DENSITY FIELD DETERMINATION IN WIND TUNNELS

Ding Hanquan, Chen Xingyi, and Chen Shouzhi
Beijing Institute of Aeronautics and Astronautics

1. INTRODUCTION

Recently, pulse double-exposure hologram technology has been used in the parameter detection of high-speed wind tunnels. That is: two instant hologram pictures of the flow field are recorded on one negative. If there is no relative movement, in all the components under the test, between the two exposures, then the interference pattern will reflect the relative parameters correctly. However, during the wind-tunnel test, because of the strong disturbance of vibrations, it is very difficult to avoid disturbance in these components; therefore there will be background fringes in the interference pattern, and this will lead to deformation. Furthermore, in order to measure and read the numbers of the interference fringes correctly, the finite-fringe method is usually used in the recording, that is: before the second exposure, one introduces a wedge-like

---

Received in March 6, 1985.

phase body, or the light is deflected by a small angle, to obtain the reference background fringes. However, it is difficult to control the orientations and distance between the background fringes and a sandwiched holograph can mend above shortages to a certain degree, but the adjustable degrees of freedom are fewer. We have developed a negative film shelf with six degrees of freedom. By using dual-holograph technology, the density distributions of the axi-symmetric shock waves with the Mach number Ma=2 are quantitatively measured in a real wind-tunnel environment, with four mathematical models [1,2]. The experimental data agrees well with the AGARD cone-like flow-chart curves.

2. THEORY

Assuming light passes through the transverse cross-section of the axi-symmetric flow field. (Fig. 1), when the flow field is in a disturbed state (the refractive index is n) and then changes to a non-disturbed state (the refractive index is n_o), the difference of the refraction index is related to the displacement, at the point (y, z), of the fringes of the interference pattern of the double-exposure holograph as follows:

$$S(y,z)=\frac{1}{\lambda}\int_{x_1}^{x_2}[n(x,y,z)-n_0]dx$$

Fig. 1. A simplified diagram for calculation of shock-wave flow field.

1-cone; 2-disturbance zone; 3-shock-wave lines; 4-shock-wave surface; 5-cone surface; 6-light.

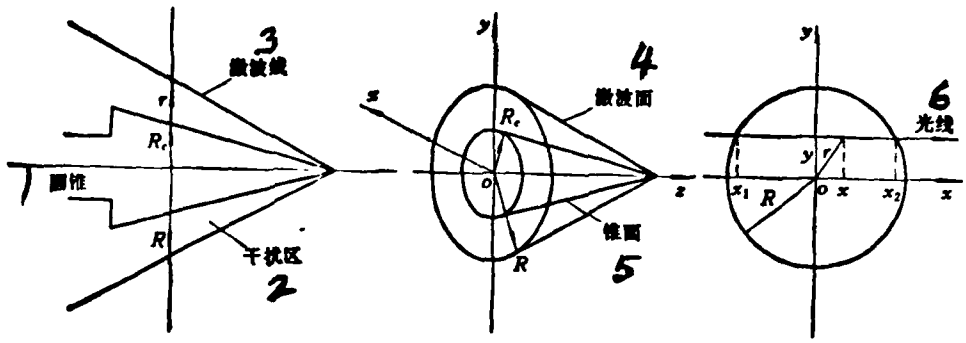

图 1　激波流场计算简图

For the cross-section of a given disturbance radius R, we have:

$$S(y)=\frac{1}{\lambda}\int_{r=y}^{R}[n(r)-n_0]\frac{dr^2}{\sqrt{r^2-y^2}} \qquad (1)$$

This is an Abel equation. The transformation of this equation is:

$$n(r)-n_0=-\frac{\lambda}{\pi}\int_{r}^{R}\frac{ds(y)}{\sqrt{y^2-r^2}} \qquad (2)$$

Assuming $n(r_i)-n_0=v_i$, From (1) and the step-function method, we obtain:

$$v_i=\frac{\frac{\lambda}{2W}S(r_i)-\sum_{\mu=i+1}^{N-1}v_\mu B(i,\mu)}{B(i,i)} \quad (i=0,1,2,\cdots,N-1) \qquad (3)$$

where

$$B(i,\mu)=\sqrt{(\mu+1)^2-i^2}-\sqrt{\mu^2-i^2}$$

According to (1) and the linear-function method, we obtain:

$$v_i=\frac{\frac{\lambda}{W}S(r_i)-\sum_{\mu=i+1}^{N-1}v_\mu B(i,\mu)}{A(i)} \quad (i=1,2,3,\cdots,N-1) \qquad (4)$$

where

$$A(i)=(i+1)\sqrt{2i+1}-i^2\ln\frac{i+1+\sqrt{2i+1}}{i}$$

$$B(i,\mu)=(\mu+1)\sqrt{(\mu+1)^2-i^2}-2\mu\sqrt{\mu^2-i^2}+(\mu-1)\sqrt{(\mu-1)^2-i^2}$$
$$+i^2\ln\frac{(\mu+\sqrt{\mu^2-i^2})^2}{[\mu+1+\sqrt{(\mu+1)^2-i^2}][\mu-1+\sqrt{(\mu-1)^2-i^2}]}$$

and

$$v_0 = \frac{\lambda}{W} S(0) - 2 \sum_{\mu=1}^{N-1} v_\mu$$

According to (2) and the plane-function method, we obtain:

$$v_i = \frac{2\lambda}{\pi W} \sum_{\mu=i}^{N-1} (S_\mu - S_{\mu+1}) \frac{\sqrt{(\mu+1)^2 - i^2} - \sqrt{\mu^2 - i^2}}{2\mu + 1} \tag{5}$$

According to (1) and the exponential-series-function method, we obtain:

$$v_i = \frac{\lambda}{2R} \sum_{n=0}^{\infty} B_n \frac{(2n+1)!!}{2^n \cdot n!} t_i^n \tag{6}$$

where $t_i = 1 - \frac{y_i^2}{R^2}$. During the calculation, n is taken up to 3.

According to the Gladstone-Dale equation, we have:

$$\rho_i - \rho_0 = v_i / K \tag{7}$$

For air and ruby lasers, the constant $K = 2.2582 \times 10^{-4} m^3/kg$.

3. EXPERIMENT

All the optical components and the film shelf for the holograph were attracted to a vibration-isolated steel-plate shelf by using magnetic bases. This makes all the components of the holographic recording, except the laser device, connected as a rigid body.

Fig. 2 is the dual-holograph shelf. It is a mechanical apparatus, which can hold two holograpic dry plates, has three degrees of freedom of transverse movement and three degrees of freedom of rotation, and can adjust the relative position of the two dry plates precisely.

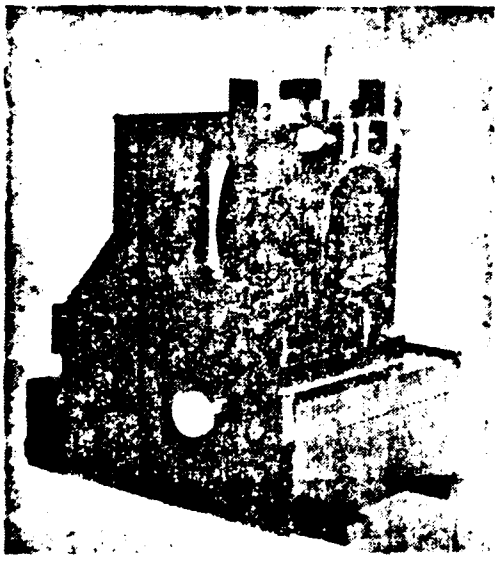

Fig. 2. The dual-holographic shelf.

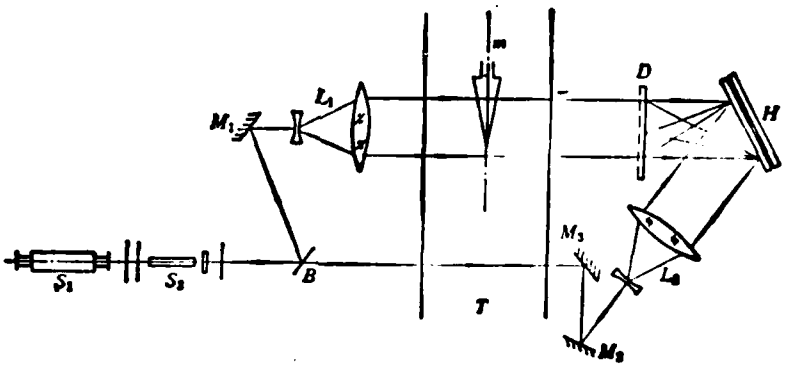

Fig. 3. The optical-path system.

S_1-He-Ne laser device; S_2-Ruby-laser device; M_1, M_2, M_3-total-reflection mirrors; L_1, L_2-collimating mirror; D-diffusing plate; B-dividing plate; m-cone model; T-wind-tunnel region; H-dry plates of holograph.

The model is a metal cone with a half angle of 15°. The axis direction is same as the direction of the incoming flows; therefore an axi-symmetric flow field is formed at the testing region.

Fig. 3 is a schematic diagram of the optical-path system. After the resonant cavity of S_2 and the optical path are adjusted by using S_1, two dry plates of the holograph are inserted to the dual-holographic shelf. An exposure is made before the wind blows and the static holographic pattern I_0 and II_0 are obtained. Then I_0 and II_0 are detached and two other dry plates are inserted. Then the wind blows and another exposure is made. Thus the holographic patterns I and II are obtained. By detaching I

(or II) and combining it with II_0 (or I_0), the dual-holographic pattern is obtained by pattern rebuilding. The II (or I) remaining on the dual-holographic shelf was exposed to the static field and then the usual double-exposure holographic pattern is obtained. It is used for comparison with the dual-holographic pattern.

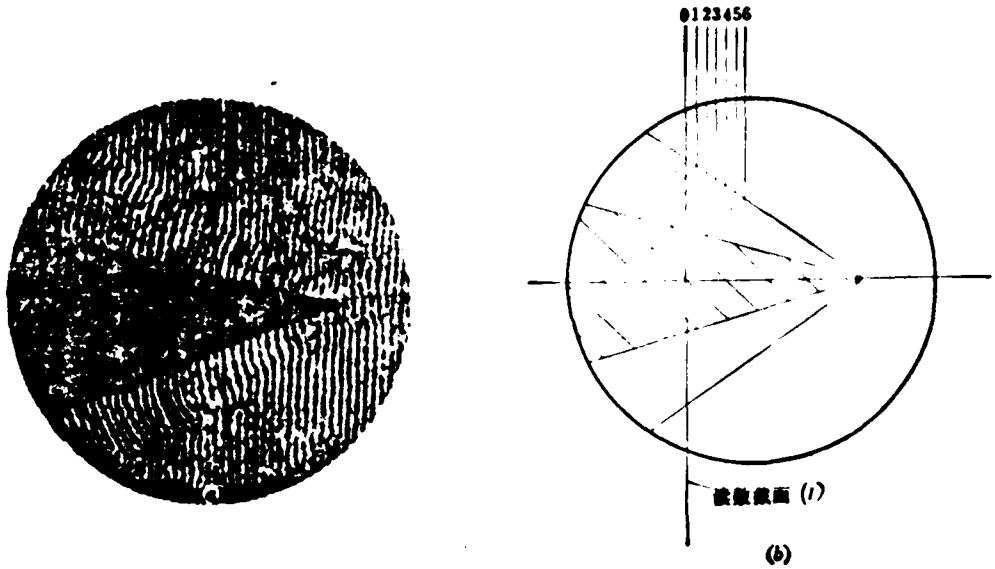

Fig. 4

(a) finite-fringe interference pattern; (b) a schematic diagram of the measurement and reading.

(1)-the cross-section of reading.

4. DATA MEASUREMENT, CALCULATION, AND RESULTS.

The cross-section for data reading was taken at the

position which is 2/3 cone length from the cone vertex (Fig. 4). The length between R_C and R were divided into N segments and altogether N+1 measuring points were taken. The distance between two neighboring measuring points is $W=(R - R_C)/N$; R_C and R are the radius of the cone at the reading point and radius of the disturbance, respectively. By using a projector, we measured R_C = 0.7100 cm, R = 1.7750 cm. With N = 20, The serial numbers i at R_C and R are 15 and 35, respectively.

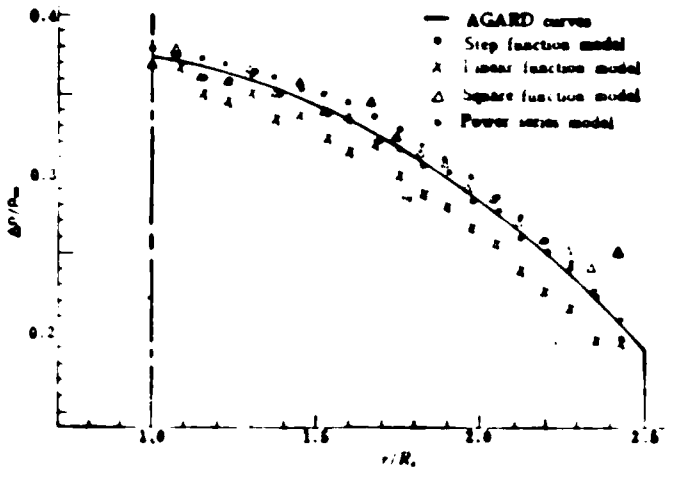

Fig. 5. A comparison of the experimental results and the AGARD curve.

Usually, we always define the displacement of the interference fringes at the intersection point of the reading cross-section and shock waves as S=0 for the calculation. As a matter of fact, this is true only at the first exposure to the static field which is an undisturbed constant-flow field, (That is: wind blows without the model, the density of the incoming flow is ρ_∞, and the refractive index is n_∞). When the static field is still (the density and refractive index of the environmental air are ρ_0 and n_0, respectively); the S value at that point should be $(n_\infty - n_0)L/\lambda$, (L is the transverse distance of the testing region). As we have defined S=0 for that point, therefore, either the static field is still or moving; we can treat it as moving, thus n_0 and ρ_0 in the above formulas should be changed into n_∞ and ρ_∞.

The interference fringes are coded according to Fig. 4(b). When the background fringes at the undisturbed region are parallel to the cross-section of the reading, the S values are at the intersecting points of each fringe of the disturbed region and this cross-section will be the code values. If there is a slope angle between the background fringes and the cross-section, the measured S' should be corrected in order to obtain the real value S.

As a results of the measurement, the total pressure

p_0=2 atm, the total temperature T_0=281 K. By using the state equation, ρ_0=2.51kg/m^3. When Ma_∞=2, by using the table, ρ_∞/ρ_0=0.2301. Then ρ_∞=0.5772 kg/m^3.

The density near the inside flank sides is:

$$\rho_n = \rho_\infty \frac{(k+1)/(k-1)}{1 + 2/(k-1) M_\infty^2 \sin^2\beta}$$

Substitute the ratio of heat capacities k=1.4, Ma_∞=2, and shock-wave angle β=33.7° into above formula, the increment at the shock-wave surface is:

$$\rho_n - \rho_\infty/\rho_\infty = \Delta\rho/\rho_\infty = 0.19$$

The experimental data are shown in Fig. 5. It can be seen that the experimental results agree well with the AGARD curve. Especially the step-function method (with simple calculations and small accumulated errors) agrees quite well. This shows that the theory and method proposed in this paper is appropriate for investigating the density distribution of axi-symmetric high-speed air flows.

REFERENCES

[1] Vest, Charles M., Holographic Interferometry, John Wiley & Sons, (1979), New York, pp. 315-320.

[2] Bradley, J. W., Density Determination from Axisymmetric Interfeograms, AIAA. J., vol. 6, No. 6, (1968), pp. 1190-1192.

Abstract

This paper presents the make use of the dual hologram interferometry for obtaining finite fringes holographic interferogram of the axisymmetric flow field with shock waves. and the density distributions computed by four mathematical models.

DISTRIBUTION LIST

DISTRIBUTION DIRECT TO RECIPIENT

ORGANIZATION	MICROFICHE
A205 DMAHTC	1
A210 DMAAC	1
B344 DIA/RTS-2C	9
C043 USAMIIA	1
C500 TRADOC	1
C509 BALLISTIC RES LAB	1
C510 R&T LABS/AVRADCOM	1
C513 ARRADCOM	1
C535 AVRADCOM/TSARCOM	1
C539 TRASANA	1
C591 FSTC	1
C619 MIA REDSTONE	4
D008 NISC	1
E053 HQ USAF/INET	1
E404 AEDC/DOF	1
E408 AFWL	1
E410 AD/IND	1
E429 SD/IND	1
P005 DOE/ISA/DDI	1
P050 CIA/OCR/ADD/SD	1
AFIT/LDE	2
FTD	1
CCN	1
NIA/PMS	1
LLNL/Code L-389	1
NASA/NST-44	1
NSA/1213/TDL	3
ASD/FTD/NIA	1

END

7-87

DTIC